

# Sensing Capabilities of Linear Elastic Cylindrical Fingers \*

Edward J. Nicolson and Ronald S. Fearing

Department of EE&CS  
University of California  
Berkeley, CA 94720

## Abstract

A linear elastic plane strain model for a cylindrical finger with a solid core and elastic surface is developed. This model is used to determine the subsurface strain impulse responses as well as pressure distributions in the contact region for indentation of the cylinder by rigid objects with friction. Singular value decomposition is used to find a reduced basis in which to analyze the shape-from-strain inversion problem. This decomposition shows that sensor depth must be small to achieve good shape sensing. However, if only contact location and applied force magnitude and direction are required, deep sensors can quickly and easily provide this information.

## 1 Introduction

Methods for inversion of tactile sensor data have used the linear elastic half plane and half space models to determine subsurface strain fields due to surface contacts. This paper develops a model specifically for cylindrical geometries and compares the predicted subsurface strain response to that of the half space model.

In [Fearing 85] it is shown how the linear elastic half space model can be used to determine contact location, shape, and force from subsurface normal strain data on a cylindrical finger. One of the open questions was the effect of the cylindrical geometry on the subsurface strain. Most recently [Ellis 92] has used a finite element model to investigate the effect of a cylindrical geometry on subsurface strain data. Their conclusions, that shape interpretation is difficult due to the high degree of similarity of subsurface strain profiles, are supported by this paper.

[Canepa et.al.] describe a neural net approach to inverting tactile sensor data. They discuss the low pass filtering effect of the rubber and the resulting limitation on shape discrimination. They point out that the shapes recognized must be restricted to those that are represented by low frequencies. This paper specifically investigates the map from surface pressure to deformed shape to determine the required frequency response for shape discrimination.

Previous work on modeling cylindrical elastic bodies [Bentall 67, Nowell 88, Poritsky 50] has focused on the surface loading and has not been concerned with the subsurface state of stress and strain. In these cases the elastic half-space model is appropriate. In our case we must know both the state for the material in the contact region at the surface, as well as beneath the surface, where sensors will be located. For subsurface strain modeling, a cylindrical model is more appropriate.

We proceed by first determining the solution to the boundary value problem of an elastic cylinder with a rigid core given the solution to the linear elastic plane problem in polar coordinates This

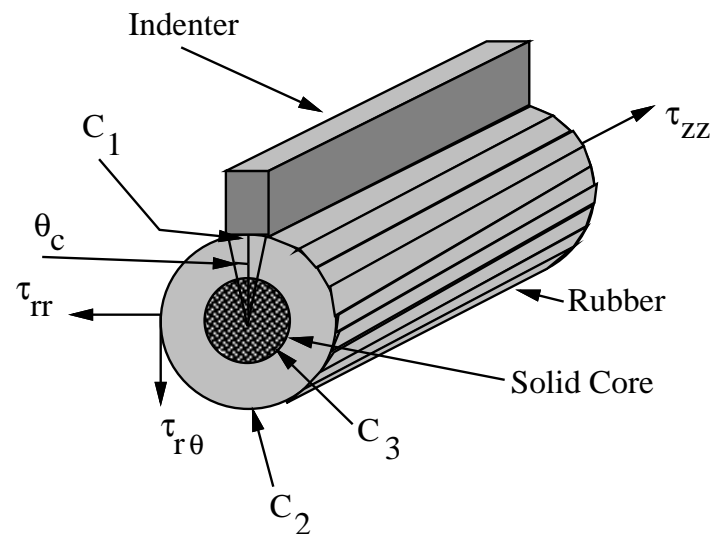


Figure 1: Cylinder in Plane Strain

model can be used to find the state of the body given the normal and tangential load in the contact region. Section 3 investigates the subsurface strain impulse response that follows directly from the model. In the next section we show how to determine the loading in the contact region given its size and the shape of the indenter in the region by solving the forward problem from indenter to state of the body. The following section investigates the properties of the solution using singular value decomposition. In section 6 we describe how sensor data may be inverted to provide the best estimate for contact location, size, load, and shape.

## 2 Solution given surface tractions

### 2.1 Problem statement

We assume that displacements are small and constant in time and that the rubber is homogeneous and isotropic. Under these assumptions we can use a linear elastostatic model. Additionally we make the assumption that the displacement field is independent of the axial direction of the cylinder, that is:

$$u_r = u_r(r, \theta) \quad u_\theta = u_\theta(r, \theta) \quad u_z = 0$$

where  $u_r$  denotes radial displacement,  $u_\theta$  denotes displacement in the angular direction, and  $u_z$  denotes axial displacement. These constitute the plane strain assumption. By making these assumptions we require the indentation to be along the length of a long cylinder.

To solve the elasticity problem we first assume that the surface traction in the radial direction,  $p(\theta)$ , and the tangential traction,  $q(\theta)$ , are known. In section 4 this assumption is removed. We also assume that the rubber layer is rigidly bonded to the solid core in the center of the cylinder. We let  $r_a$  be the radius of the core and  $r_b$  be the outer radius. The contact is centered at  $\theta_c$  and

\*This work was funded in part by: NSF PYI Grant IRI-9157051, A National Needs Fellowship, and NSF grant IRI-9114446.

has a total width, in radians, of  $\theta_w$ . Referring to Figure 1, the boundary conditions may be stated as follows:

$$C_1 : \tau_{rr} = p(\theta), \quad \tau_{r\theta} = q(\theta)$$

$$C_2 : \tau_{rr} = p(\theta) = 0, \quad \tau_{r\theta} = q(\theta) = 0$$

$$C_3 : u_r = 0, \quad u_\theta = 0$$

where:

$$q(\theta) = \begin{cases} \mu_f p(\theta) & \text{full sliding} \\ < \mu_f p(\theta) & \text{adhesion} \end{cases}$$

We have used  $C_1$  to indicate the contact region. In this region non-zero tractions, both radial and tangential, are exerted by the indenter on the elastic surface. In  $C_2$ , the region outside the contact on the surface, there are zero tractions. On  $C_3$  the elastic region is bonded to the rigid core. Note that the functions  $p(\theta)$  and  $q(\theta)$  are assumed to be zero outside the contact region. With these mixed-mixed boundary conditions the problem is well posed.

## 2.2 Fourier series decomposition

As we are using linear elasticity to solve this problem we may use the principle of superposition to sum independent partial solutions. The sum of these partial solutions gives the desired solution. Since all the partial solutions will be periodic in  $\theta$  with period  $2\pi$ , a fourier series decomposition is natural. Using a trigonometric fourier series we can write the surface tractions as follows:

$$\begin{aligned} \tau_{rr}(r_b, \theta) &= p(\theta) = p_0 + \sum_{k=1}^{\infty} p_k^c \cos k\theta + \sum_{k=1}^{\infty} p_k^s \sin k\theta \\ \tau_{r\theta}(r_b, \theta) &= q(\theta) = q_0 + \sum_{k=1}^{\infty} q_k^c \cos k\theta + \sum_{k=1}^{\infty} q_k^s \sin k\theta \end{aligned}$$

We desire a solution of the form:

$$\begin{aligned} \tau_{rr}(r, \theta) &= \tau_{rr_0}(r) + \sum_{k=1}^{\infty} \tau_{rrk}^c(r) \cos k\theta + \sum_{k=1}^{\infty} \tau_{rrk}^s(r) \sin k\theta \\ \tau_{r\theta}(r, \theta) &= \tau_{r\theta_0}(r) + \sum_{k=1}^{\infty} \tau_{r\theta k}^c(r) \cos k\theta + \sum_{k=1}^{\infty} \tau_{r\theta k}^s(r) \sin k\theta \\ u_r(r, \theta) &= u_{r_0}(r) + \sum_{k=1}^{\infty} u_{rk}^c(r) \cos k\theta + \sum_{k=1}^{\infty} u_{rk}^s(r) \sin k\theta \\ u_\theta(r, \theta) &= u_{\theta_0}(r) + \sum_{k=1}^{\infty} u_{\theta k}^c(r) \cos k\theta + \sum_{k=1}^{\infty} u_{\theta k}^s(r) \sin k\theta \end{aligned}$$

By solving the elasticity problem for each  $k$  and summing we solve the complete problem. In this paper we have also computed the fourier series coefficients for the normal strain,  $e_{rrn}$  as  $e_{rr_0}$ ,  $e_{rrn}^s$  and  $e_{rrn}^c$ . In polar coordinates the shear strain can be computed directly from the shear stress with  $e_{r\theta}(r, \theta) = \frac{1}{2\mu} \tau_{r\theta}(r, \theta)$ .

## 2.3 Plane-strain solutions for cylindrical coordinates using Airy functions

We use an Airy function in polar coordinates to find the solution that satisfies the 3 basic equations of linear elastostatics: strain-displacement, stress-strain, and the stress equations

of equilibrium. The derivation of the following may be found in [Sokolnikoff]. [Timoshenko 70] provides an overview of two dimensional problems in polar coordinates. Given a function  $\phi(r, \theta)$  satisfying:

$$\nabla^4 \phi = 0$$

$$\nabla^2 = \frac{\partial^2}{\partial r^2} + \frac{1}{r} \frac{\partial}{\partial r} + \frac{1}{r^2} \frac{\partial^2}{\partial \theta^2}$$

then  $\phi$  generates the plane strain solution:

$$\tau_{rr} = \frac{1}{r} \frac{\partial \phi}{\partial r} + \frac{1}{r^2} \frac{\partial^2 \phi}{\partial \theta^2}$$

$$\tau_{r\theta} = \frac{1}{r^2} \frac{\partial \phi}{\partial \theta} - \frac{1}{r} \frac{\partial^2 \phi}{\partial r \partial \theta}$$

$$L = \nabla^2 \phi, \quad f(z) = L + iM, \quad z = r e^{i\theta}$$

$$g(z) = l + im = \int f(\eta) d\eta$$

$$2\mu u_r = -\frac{\partial \phi}{\partial r} + (1 - \sigma)(l \cos \theta + m \sin \theta) + a_1^o \cos \theta + a_2^o \sin \theta$$

$$2\mu u_\theta = -\frac{1}{r} \frac{\partial \phi}{\partial \theta} + (1 - \sigma)(-l \sin \theta + m \cos \theta) - a_1^o \sin \theta + a_2^o \cos \theta - w^o r$$

Here  $\mu$  is the shear modulus and  $\sigma$  is Poisson's ratio. These parameters are related to the more well known Young's modulus,  $E$ , by  $E = 2\mu(1 + \sigma)$ . The function  $M$  is the conjugate harmonic to  $L$ . The details of the derivation  $l$ ,  $m$ , and  $M$  can be found in a standard text covering complex analysis. The following set of Airy functions, pointed out by [Bogy], will generate the required set of solutions.

$$\begin{aligned} \phi^0 &= a_0 \ln r + b_0 r^2 + c_0 \theta \\ \phi^1 &= \left( \frac{a_1}{r} + b_1 r^3 + c_1 r \ln r \right) \begin{Bmatrix} \sin \theta \\ \cos \theta \end{Bmatrix} + d_1 r \theta \begin{Bmatrix} \cos \theta \\ \sin \theta \end{Bmatrix} \\ \phi^n &= (a_n r^n + b_n r^{-n} + c_n r^{2+n} + d_n r^{2-n}) \begin{Bmatrix} \sin n\theta \\ \cos n\theta \end{Bmatrix} \end{aligned}$$

The above set of Airy functions can be shown to be a complete set of solutions. Given this set we now must solve for the constants,  $a_n$ ,  $b_n$ ,  $c_n$ ,  $d_n$ ,  $a_1^o$ ,  $a_2^o$ , and  $w^o$  given the boundary conditions. We do not give the explicit formulas for these constants, but instead give the equations for the fourier series coefficients which are based on these constants.

## 2.4 Solutions

By substituting in the boundary conditions, the constant coefficients in the previous equations are solved for each  $n$ . It is useful to define the following:

$$\alpha = \frac{r_a}{r_b}, \quad \beta = \frac{r_a}{r}, \quad \gamma = \frac{r}{r_b}, \quad \hat{\sigma} = 3 - 4\sigma$$

Note that  $\alpha$ ,  $\beta$ , and  $\gamma$  are all less than 1.

### 2.4.1 $n = 0$

For  $n = 0$  the following solution is obtained.

$$\begin{bmatrix} \tau_{rr_0}(r) \\ \tau_{r\theta_0}(r) \\ u_{r_0}(r) \\ u_{\theta_0}(r) \\ e_{rr_0}(r) \end{bmatrix} = \begin{bmatrix} \frac{2+\beta^2(-1+\sigma)}{2+\alpha^2(-1+\sigma)} & 0 \\ 0 & \gamma^{-2} \\ \frac{\gamma r_b(-1+\sigma)(1-\beta^2)}{2\mu(2+\alpha^2(-1+\sigma))} & 0 \\ 0 & \frac{r_b(1-\beta^2)}{2\alpha\beta\mu} \\ \frac{(1+\beta^2)(1-\sigma)}{2\mu(-2+\alpha^2(1-\sigma))} & 0 \end{bmatrix} \begin{bmatrix} p_0 \\ q_0 \end{bmatrix} \quad (1)$$

We should point out here that the shear stress and shear strain at  $r_a$  due to a constant shear load at  $r_b$  increase as  $r_b^2$ . This is important to consider when designing rubber coated fingers. Also we note that  $u_{\theta_0}(r)$  indicates how much rotation occurs about the axis of the cylinder due to a tangential load. Finally we note that for incompressible materials where  $\sigma = \frac{1}{2}$  there is no radial displacement due to a constant load applied normally over the complete surface of the finger.

### 2.4.2 $n = 1$

For  $n = 1$  the solution is more involved, but simplifies to the following form ( $A_1$  and  $B_1$  are given in the Appendix):

$$\begin{bmatrix} \tau_{rr_1}^s(r) \\ \tau_{r\theta_1}^c(r) \\ u_{r_1}^s(r) \\ u_{\theta_1}^c(r) \\ e_{rr_1}^s(r) \end{bmatrix} = B_1(r)q_1^c + A_1(r)(p_1^s + q_1^c)$$

$$\begin{bmatrix} \tau_{rr_1}^c(r) \\ -\tau_{r\theta_1}^s(r) \\ u_{r_1}^c(r) \\ -u_{\theta_1}^s(r) \\ e_{rr_1}^c(r) \end{bmatrix} = -B_1(r)q_1^s + A_1(r)(p_1^c - q_1^s) \quad (2)$$

### 2.4.3 $n \geq 2$

For  $n \geq 2$  the form of the solution is similar:

$$\begin{bmatrix} \tau_{rr_n}^s(r) \\ \tau_{r\theta_n}^c(r) \\ u_{r_n}^s(r) \\ u_{\theta_n}^c(r) \\ e_{rr_n}^s(r) \end{bmatrix} = \frac{1}{\delta_n} A_n(r) B_n L \begin{bmatrix} p_n^s \\ q_n^c \end{bmatrix}$$

$$\begin{bmatrix} \tau_{rr_n}^c(r) \\ -\tau_{r\theta_n}^s(r) \\ u_{r_n}^c(r) \\ -u_{\theta_n}^s(r) \\ e_{rr_n}^c(r) \end{bmatrix} = \frac{1}{\delta_n} A_n(r) B_n L \begin{bmatrix} p_n^c \\ -q_n^s \end{bmatrix} \quad (3)$$

A quick glance at the above solutions reveals that the sine terms for  $e_{rr}$ , the normal strain, and the cosine terms for  $e_{r\theta}$ , the shear strain, depend only on the sine terms for the normal surface pressures and the cosine terms for the tangential surface pressures. This is an important property which has implications for indenter shape sensing.

## 3 Impulse and frequency response

If the cylinder is indented with a sharp edge, then the loading will be distributed over a very small area. In terms of the model



Figure 2: Surface and subsurface displacements due to a concentrated load applied at 45 degrees to the surface. It is assumed that  $\mu_f \geq 1.0$ . The dashed lines are drawn between the undeformed and deformed positions. The units are meters. The center of the cylinder is located far off to the left hand side of the page.

parameters,  $\theta_w$  will be very small. The fourier series coefficients for such an impulsive load with pressure magnitude  $\lambda \frac{N}{m^2}$  applied at an angle  $\phi$  from the surface normal (assuming no slip) at contact location  $\theta_c$  are:

$$p_0 = \frac{\lambda}{2\pi} \cos \phi$$

$$p_k^c = \frac{\lambda}{\pi} \cos(k\theta_c) \cos \phi$$

$$p_k^s = \frac{\lambda}{\pi} \sin(k\theta_c) \cos \phi$$

$$q_0 = \frac{\lambda}{2\pi} \sin \phi$$

$$q_k^c = \frac{\lambda}{\pi} \cos(k\theta_c) \sin \phi$$

$$q_k^s = \frac{\lambda}{\pi} \sin(k\theta_c) \sin \phi$$

To allow comparison with the cylindrical model to the half plane used in [Fearing 90] we use the same parameters.

$$\mu = 8.3 * 10^4 \frac{N}{m^2} \quad \sigma = 0.5$$

$$r_a = 8.9mm \quad r_b = 12.7mm$$

Additionally we assume that the sensors are located at radius  $r_s = r_a + 0.5mm$ .

Figure 2 shows the displacement field due to a knife edge applied at 45 degrees to the surface of the cylinder at  $\theta_c = 0$ . The subsurface displacement field makes it immediately clear that a large degree of spatial frequency filtering is occurring. To get a better idea of the type of filtering, Figure 3 shows the shear and normal strain coefficients,  $e_{rr_k}$  and  $e_{r\theta_k}$ , as they vary with the index  $k$ . This plot is in effect the *spatial frequency* response due to the rubber layer. That is, since the frequency spectrum

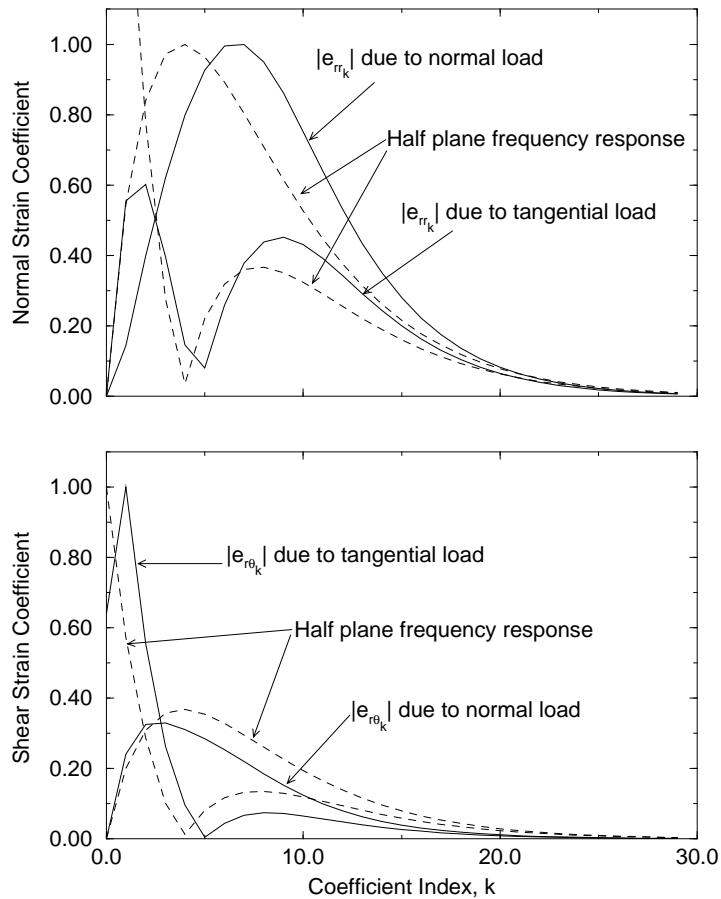


Figure 3: Subsurface strain frequency responses for the cylindrical and half plane models.

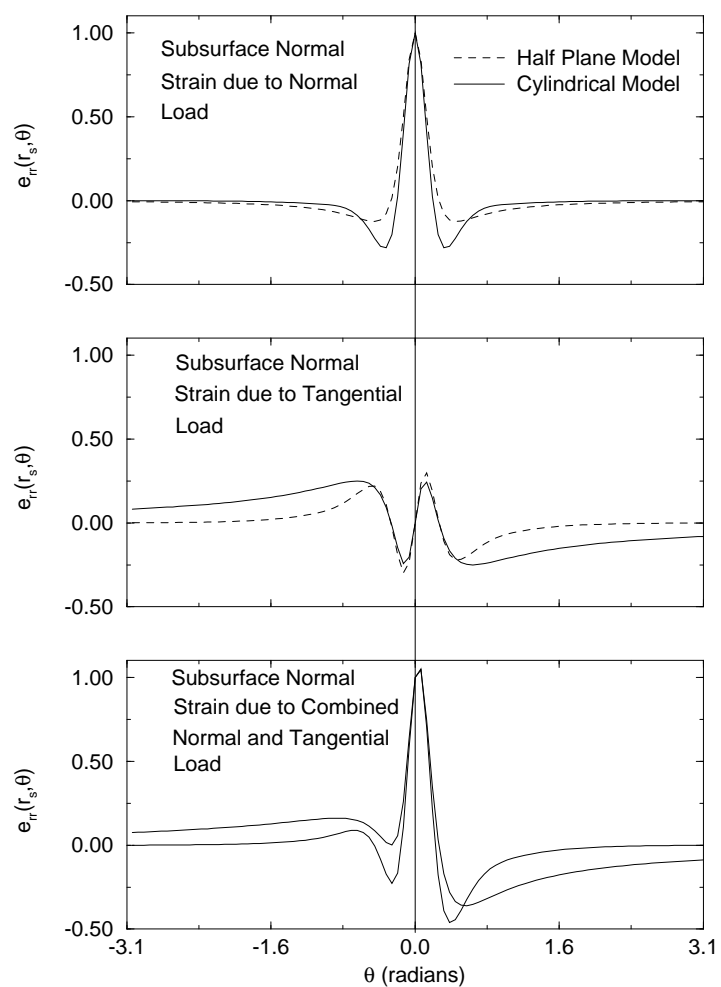


Figure 4: Subsurface normal strain impulse response.

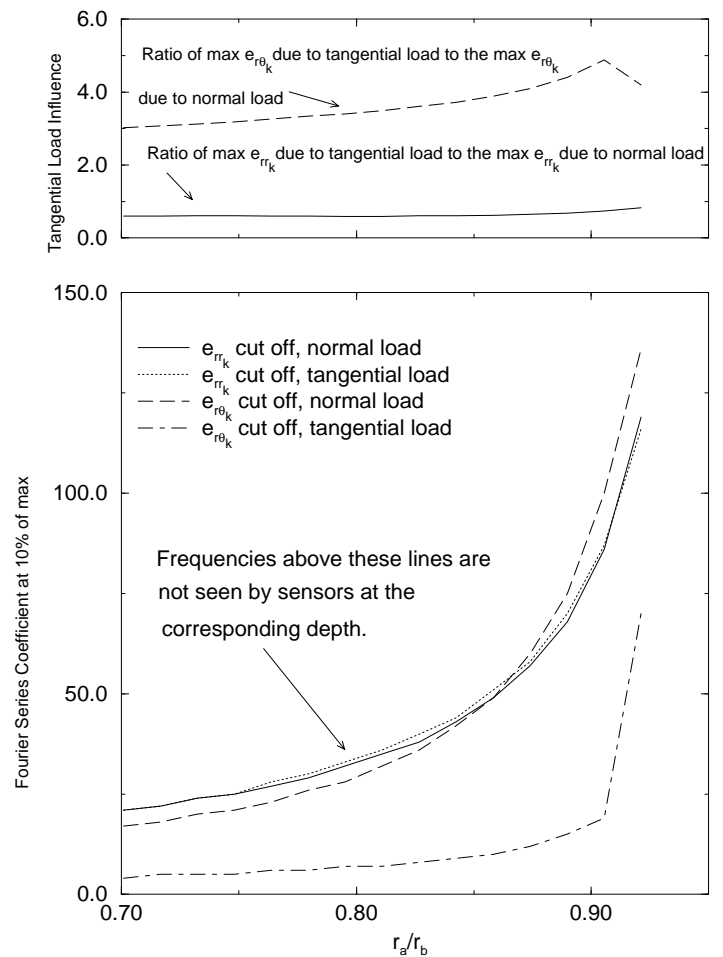


Figure 5: Variation in filter cut-off with  $\alpha = \frac{r_a}{r_b}$ . Sensors are located at  $r_s = r_a + 0.5\text{mm}$ .

of the loading was flat, Figure 3 shows the relative effect of each loading frequency component on the corresponding frequency of the subsurface strain. We note that  $e_{rrk}$  and  $e_{r\theta k}$  drop off to below 10 percent of their maximum value by the 20th coefficient. Due to this high degree of low pass filtering, the subsurface normal strain, as shown in Figure 4, does not change perceptibly with contacts that vary in shape frequencies above the cut-off frequency.

Figures 3 and 4 also show the comparable frequency and impulse response for the plane strain half plane model [Johnson 85, Fearing 85]. The plots have been normalized to the peak value. In both figures the response due to normal and tangential loading has been separated to show the relative effect of normal and tangential loads on the normal and shear strain. The half space model shows a larger degree of filtering from normal loads the normal strain given the same rubber thickness as is apparent from the smaller side lobes in the impulse response and the smaller cut-off frequency in the frequency response. In figure 4 we see that the effect of tangential loading on normal strain is similar until the effect of the cylinder's curvature becomes apparent at  $\theta = .4$  radians.

In Figure 3 we see the dominance at low frequencies of the tangential loading on the shear strain. Whereas the normal strain due to the normal and tangential loading are just a factor of 2 in comparative magnitude and have a similarly shaped frequency response, the shear strain is affected by a factor of 3 more by the tangential load than the normal load and the frequency response drops off much more sharply.

So far we have only discussed the filtering effects for one set of radii parameters. Figure 5 shows how the cut-off frequencies and tangential load influence vary as  $\alpha = \frac{r_a}{r_b}$  approaches 1.0. As you can see, the cut-off frequency increases exponentially. We note, however, that  $e_{r\theta}$  is filtered to only 10 cycles per revolution when  $\alpha$  is as large as 0.85. This indicates that shear strain sensing may be used as a good indicator of tangential load, but not of contact

shape in the presence of tangential loading.

#### 4 Determining $p(\theta)$ and $q(\theta)$

The model developed in the previous section assumed that the normal and tangential surface stresses were known. If we were considering only frictionless contacts then the standard Hertz contact model could be used to determine the parabolic pressure distribution. However if we wish to analyze the influence of a contact with friction we must determine the combination of tangential and normal loading that give the same shape of deformation in the contact region as the indenter.

Since we want to determine  $p(\theta)$  and  $q(\theta)$  given an indenter shape, load, and location we need to invert the model derived in section 2. Unfortunately these equations do not adapt easily to the shape and load formulation, instead we will state the equivalent constraints: indenter shape, location ( $\theta_c$ ), and the size of the area of contact ( $\theta_w$ ). The slope of the deformed surface is given by:

$$s(\theta) = \left. \frac{\partial u_r}{\partial \theta} \right|_{(r_b, \theta)} \quad (4)$$

With the correct loading,  $s(\theta)$  will be the same as the slope of the indenter in the contact region.

At this point we must resort to numerical techniques and truncate the fourier series. If we wish  $n_{\max}$  periods of the highest frequency in the series in the contact region then we must compute the fourier series up to:

$$n > \frac{2\pi n_{\max}}{\theta_w}$$

Since our main concern is with sensor data inversion, we can be satisfied with picking our  $n = n_c = 300$  so that for a 2 mm contact we will have 7.6 periods of the highest frequency component in the contact region. This will provide an adequate approximation of the contact shape while easily including all the frequencies that will be sensed below the surface.

We start by computing the slope of the indenter at  $n_p > (2n_c + 2)$  points in the contact region as:

$$\theta_i = \theta_c - \frac{2(i - \frac{n_p}{2})\theta_w}{n_p} \quad (5)$$

$$s_i = s(\theta_i) \quad (6)$$

$$0 \leq i \leq n_p$$

and let  $\mathbf{s}$  be the vector corresponding to  $s_i$ .

We next compute a  $n_p \times (4n_c + 2)$  real valued matrix which maps from the fourier series coefficients of the normal and tangential tractions (truncated to the frequency  $n_c\theta$ ) to the displacement slope at each point in the contact region. To do this we first compute the fourier series coefficients for surface normal and tangential displacements due to unit normal and tangential loads at each frequency as:

$$\begin{aligned} \hat{u}_{rr_0} &= \frac{\gamma r_b (-1 + \hat{\sigma}) (1 - \beta^2)}{2\mu (2 + \alpha^2 (-1 + \hat{\sigma}))} \\ \hat{u}_{r\theta_0} &= 0 \\ \hat{u}_{rr_j}^s &= \hat{u}_{rr_j}^c = \frac{1}{\delta_n} A_n(r_b) B_n L \begin{bmatrix} 1 \\ 0 \end{bmatrix} \\ \hat{u}_{r\theta_j}^s &= \frac{1}{\delta_n} A_n(r_b) B_n L \begin{bmatrix} 0 \\ -1 \end{bmatrix} \\ \hat{u}_{r\theta_j}^c &= \frac{1}{\delta_n} A_n(r_b) B_n L \begin{bmatrix} 0 \\ 1 \end{bmatrix} \end{aligned} \quad (7)$$

Coefficients for  $j = 1$  can be computed similarly. Now, for  $j \neq 1$  and  $j \neq 2n_c + 2$ ,  $\mathbf{T}$  is given by:

$$T_{ij} = \begin{cases} \hat{u}_{rr_k}^s k \cos(k\theta_i) & j \text{ odd } j < 2n_c + 2 \\ -\hat{u}_{rr_k}^c k \sin(k\theta_i) & j \text{ even } j < 2n_c + 2 \\ \hat{u}_{r\theta_k}^s k \cos(k\theta_i) & j \text{ odd } j > 2n_c + 2 \\ -\hat{u}_{r\theta_k}^c k \sin(k\theta_i) & j \text{ even } j > 2n_c + 2 \end{cases} \quad (8)$$

where  $k = \text{int}((j - 1)/2)$ . The first and  $2n_c + 2$  column of  $\mathbf{T}$  are given by:

$$T_{i1} = \hat{u}_{rr_0} \quad (9)$$

$$T_{i(2n_c+2)} = \hat{u}_{r\theta_0} \quad (10)$$

With  $\mathbf{T}$  constructed as above, it may be applied to a vector of fourier series coefficients for normal and tangential tractions to give the slope in the contact region. Let  $\mathbf{s}$  be the vector associated with  $s_i$ ,  $\mathbf{p}$  be the vector associated with  $p_j$ , and  $\mathbf{q}$  be the vector associated with  $q_j$ . Then we have:

$$\mathbf{s} = \mathbf{T} \begin{bmatrix} \mathbf{p} \\ \mathbf{q} \end{bmatrix}. \quad (11)$$

If we were simply to invert  $\mathbf{T}$  to determine the fourier coefficients given the slope in the contact region then we would have no guarantee that the pressures would be zero outside the contact region. To solve this problem we convolve the  $p_k$  and  $q_k$  with the coefficients for a Hanning window truncated to  $n_c/2$  before multiplying them by  $\mathbf{T}$ . Call this convolution matrix  $\mathbf{C}$ .  $\mathbf{C}$  has dimensions  $(4n_c + 2) \times (2n_c + 2)$ . We have:

$$\begin{bmatrix} \mathbf{p} \\ \mathbf{q} \end{bmatrix} = \mathbf{C} \begin{bmatrix} \tilde{\mathbf{p}} \\ \tilde{\mathbf{q}} \end{bmatrix} \quad (12)$$

$$\mathbf{s} = \mathbf{TC} \begin{bmatrix} \tilde{\mathbf{p}} \\ \tilde{\mathbf{q}} \end{bmatrix} \quad (13)$$

We have used the  $\tilde{\phantom{x}}$  symbol to note the fact that the coefficients  $\tilde{\mathbf{p}}$  and  $\tilde{\mathbf{q}}$  will have non-zero pressure outside the contact region, but  $\mathbf{p}$  and  $\mathbf{q}$  will have minimal energy outside the contact region due to the windowing.

A straight inversion of  $\mathbf{T}$  would be numerically unstable, thus we have used singular value decomposition to compute its pseudo-inverse as:

$$\mathbf{TC} = \mathbf{U}^T \mathbf{\Sigma} \mathbf{V} \quad (14)$$

$$(\mathbf{TC})^+ = \mathbf{V}^T \mathbf{\Sigma}^{-1} \mathbf{U} \quad (15)$$

where  $\mathbf{\Sigma}$  is diagonal and  $\mathbf{U}$  and  $\mathbf{V}$  correspond to pure rotations. This decomposition provides valuable insight into the shape to pressure map that will be discussed in the next section.

We illustrate the use of the inverse with the following example. If we wish to model the frictionless contact of a flat surface with the cylinder with a contact length of 2mm then we choose:

$$\begin{aligned} \theta_w &= \frac{2.0}{r_b} \\ s_i &= r_b \theta_i \end{aligned}$$

and compute the surface tractions as:

$$\begin{bmatrix} \mathbf{p} \\ \mathbf{q} \end{bmatrix} = \mathbf{CV}^T \mathbf{\Sigma}^{-1} \mathbf{U} \mathbf{s}. \quad (16)$$

The resulting displacement field is shown in Figure 6 and the resulting surface stress is shown in Figure 7. As would be expected, the surface stress is the parabolic stress given by a Hertz contact.

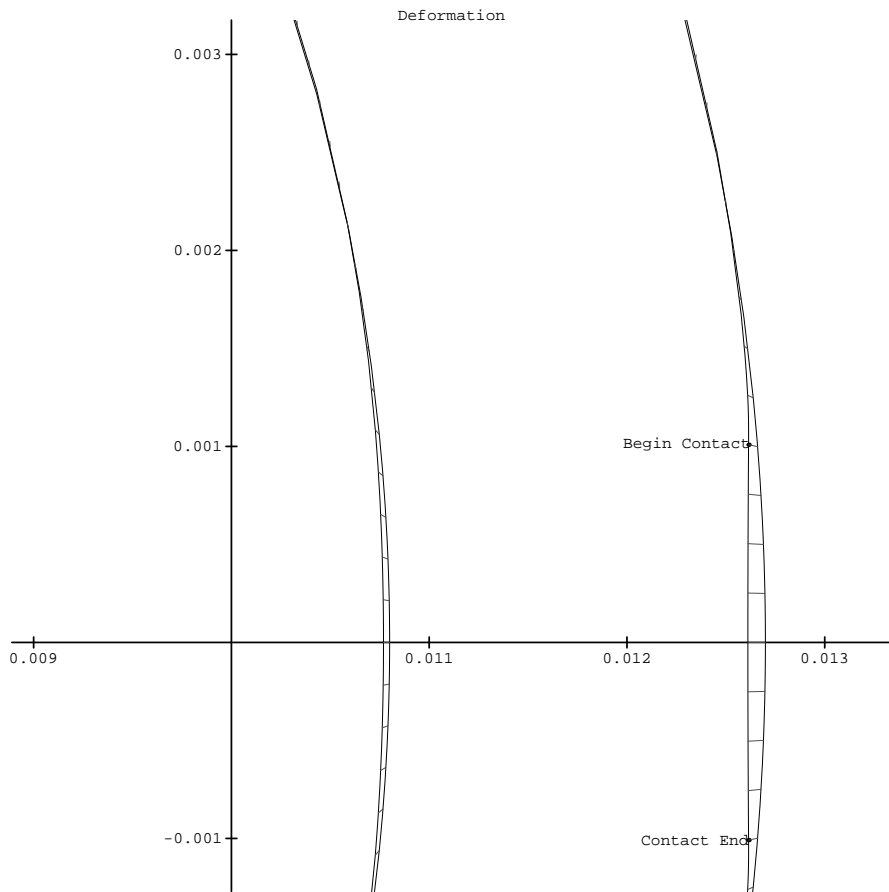


Figure 6: Displacement field for a flat frictionless indenter.

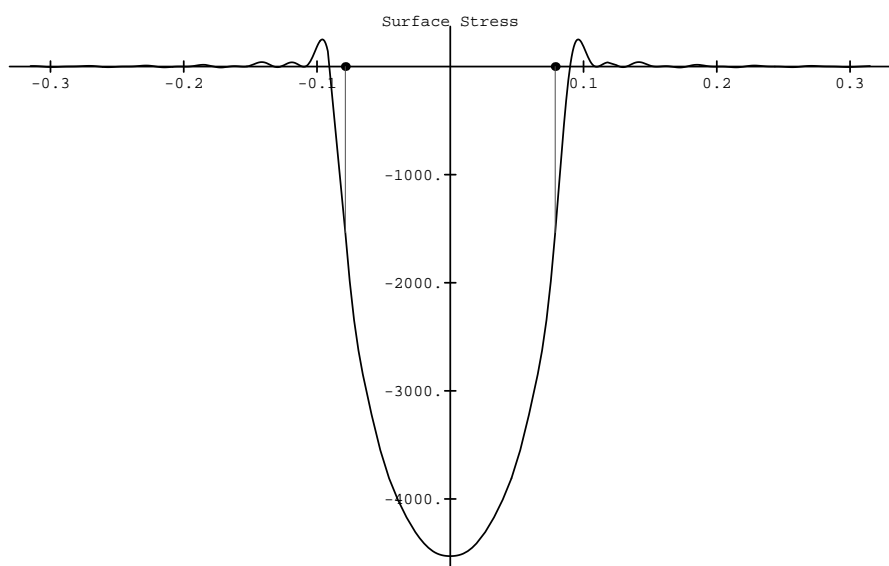


Figure 7: Surface stress for flat frictionless indenter. The dotted lines indicate the bounds of the contact region.

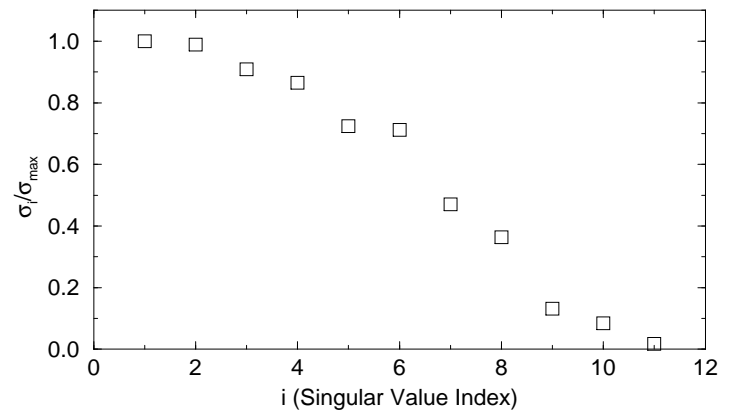


Figure 8: Magnitudes of singular values of  $\mathbf{TC}$ .

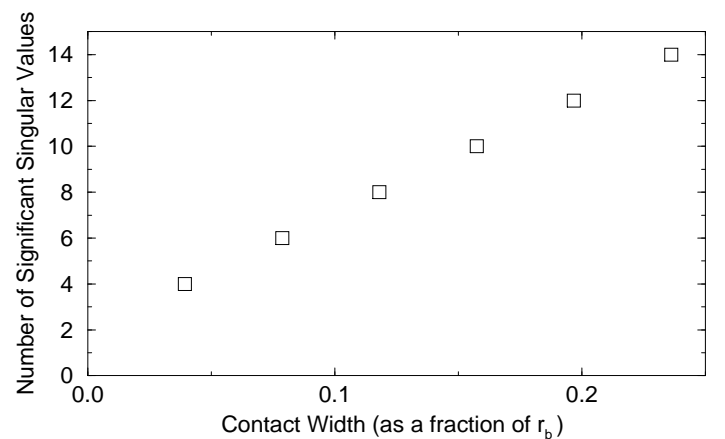


Figure 9: Variation in number of singular values of  $\mathbf{TC}$  with contact width

## 5 Bandlimited shape interpretation

The magnitudes of the singular values and the rows of the matrices  $\mathbf{U}$  and  $\mathbf{V}$  can be used to determine the ability of subsurface strain sensors to discriminate different shaped indenters on the surface. With  $r_a, r_s, r_b$ , and  $\theta_w$  as before, the matrix  $\mathbf{TC}$  has 11 singular values with relative magnitude greater than 1/100 of the maximum singular value. Figure 8 shows the magnitudes.

In fact there are only 8 singular values with magnitude greater than 1/10 of the maximum singular value. The singular values with smaller magnitude may be discarded since they will have little influence on the slope vector  $\mathbf{s}$ . That is, pressure distributions with coefficients orthogonal to the *rows* of  $\mathbf{V}$  corresponding to the 8 most significant singular values will have a very small effect on the slope.

The small number of singular values is not surprising as it corresponds closely to the number of full periods of the highest frequency that we modeled that can occur in the contact region ( $n_c = 300$ ,  $\theta_w = 0.16$ , number of periods = 7.6). Figure 9 shows how the number of singular values varies with contact width for  $n_c = 300$ .

The singular value decomposition gives us more than just a reduction in the problem size, it also helps us understand the shape to pressure map. The rows of  $\mathbf{U}$  and  $\mathbf{V}$  give matched pairs of pressure coefficients and shape in the contact region. Figure 10 plots the first four rows of the matrices giving the most significant directions in the shape to pressure map. The following relationships are immediately clear:

$$\text{Odd Shape} \Leftrightarrow \text{Even Slope} \Leftrightarrow \text{Odd Pressure}$$

$$\text{Even Shape} \Leftrightarrow \text{Odd Slope} \Leftrightarrow \text{Even Pressure}$$

What is most important is that the spectrum of the odd shapes is near zero at the low frequencies. Given the sensor parameters of [Fearing 90] it would be very difficult to sense the odd part of the

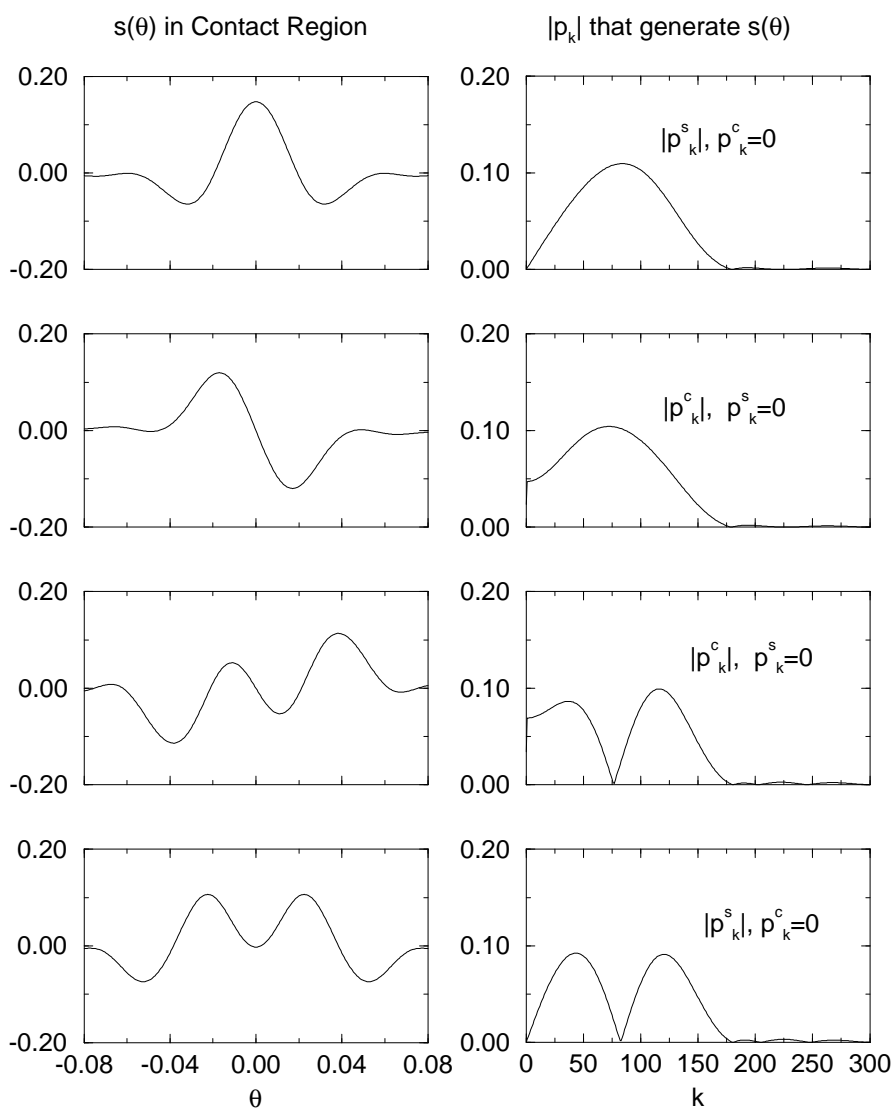


Figure 10: Basis functions

shape since, as Figure 3 shows, that information will be filtered out. In effect the low frequency component of the odd part of the shape can not be sensed without putting the sensors closer to the surface, with  $\alpha > 0.85$ .

## 6 Conclusions and future directions

We have presented a linear elastic model for a cylindrical sensor and investigated the subsurface strain frequency responses to estimate the sensor performance. We can conclude that localization and force information is good and may be obtained with just a few data points. It does not appear that shear strain sensing will aid particularly in the inversion process as it will be dominated at the low frequencies by the tangential loading. For good shape discrimination the sensors must be put close to the surface, at  $\alpha > 0.85$ , or the sensors must be highly noise free and accurate to at least 1 percent to detect the high frequency information.

A sensor is being constructed based on the design of [Fearing 90] to test the validity of this model. We expect to find that localization and detection of force magnitude and direction will be fast and well posed. The first sensor will have  $\alpha = 0.7$  which will induce sufficient low pass filtering that the subsurface normal strain will depend almost exclusively on the location of the contact and the tangential load. Both of the impulse responses, as shown in figure 4, will vary little with indenter shape, so by simply scaling and shifting the two responses to fit the data the location and direction of force may be found from 3 data points. This will require a minimum of 16 sensors around the circumference. With this sensor our shape discrimination from single touches will be limited. We will investigate other sensor designs that will maximize shape information.

## References

- [Bentall 67] R.H. Bentall and K.L. Johnson, "Slip in the Rolling Contact of Two Dissimilar Elastic Rollers," *Int. Journal Mechanical Sciences*, Vol. 9, 1967, pp. 389-404.
- [Bogy] D.B. Bogy, Lecture Notes from Course on Linear Elasticity, U.C. Berkeley Mechanical Engineering Department, Spring 1991.
- [Canepa et.al.] G. Canepa, M. Morabito, D. De Rossi, A. Caiti, T. Parisini, "Shape from touch by a neural net," *Proc. 1992 IEEE Conf. on Robotics and Automation*, Nice, France, May, 1992, pp. 2075-2080.
- [Ellis 92] R.E. Ellis and S.L. Ricker, "Some Implications of Solid Mechanics for Tactile Feedback in Teleoperation," *SPIE Proceedings 1833*, Boston, MA, November, 1992.
- [Fearing 85] R.S. Fearing and J.M. Hollerbach, "Basic Solid Mechanics for tactile Sensing," *The Int. Journal of Robotics Research*, Vol. 4, No. 3, Fall 1985, pp. 40-54.
- [Fearing 90] R.S. Fearing, "Tactile Sensing Mechanisms," *The Int. Journal of Robotics Research*, Vol. 9, No. 3, June 1990, pp. 3-23.
- [Johnson 85] K.L. Johnson, *Contact Mechanics*, Cambridge University Press, Cambridge, 1985.
- [Love 34] A.E.H. Love, *A Treatise on the Mathematical Theory of Elasticity*, Cambridge University Press, Cambridge, 1934, pp 89-91.
- [Nowell 88] D. Nowell and D.A. Hills, "Tractive Rolling of Tyred Cylinders," *Int. Journal of Mechanical Sciences*, Vol. 30, No. 12, 1988, pp. 945-957.
- [Nowlin 92] W.C. Nowlin, "Experimental Results on Bayesian Algorithms for Interpreting Tactile Sensing Data," *Proc. 1991 IEEE Conf. on Robotics and Automation*, Sacramento, CA, April, 1991, pp. 378-383.
- [Poritsky 50] H. Poritsky, "Stresses and Deflections of Cylindrical Bodies in Contact With Application to Contact of Gears and Locomotive Wheels," *Journal of Applied Mechanics*, June 1950, pp. 191-201.
- [Sokolnikoff] I.S. Sokolnikoff, "Mathematical Theory of Elasticity," Notes from Summer session for advanced instruction and research in mechanics. June 23-September 13, 1941, Robert E. Krieger Publishing Company, Malabar, Florida, 1941.
- [Timoshenko 70] S.P. Timoshenko and J.N. Goodier, *Theory of Elasticity, 3d ed.*, New York, McGraw-Hill, 1970, pp. 168-187.

## 7 Appendix: Solutions

$$B_1(r) = \begin{bmatrix} -\frac{(\gamma + \alpha\beta^3\hat{\sigma})}{1 + \alpha^4\hat{\sigma}} \\ \frac{(\gamma + \alpha\beta^3\hat{\sigma})}{1 + \alpha^4\hat{\sigma}} \\ \frac{r_b(\gamma^2(2 - \hat{\sigma}) - \alpha^2(2 - \beta^2\hat{\sigma}))}{4\mu(1 + \alpha^4\hat{\sigma})} \\ \frac{r_b(\gamma^2(2 + \hat{\sigma}) - \alpha^2(2 + \beta^2\hat{\sigma}))}{4\mu(1 + \alpha^4\hat{\sigma})} \\ \frac{\gamma(2 - \hat{\sigma} - \beta^4\hat{\sigma})}{2\mu(1 + \alpha^4\hat{\sigma})} \end{bmatrix}$$

$$A_1(r) = \begin{bmatrix} \frac{1}{2\gamma(1 + \hat{\sigma})} \left( 3 + \hat{\sigma} + \frac{2(-\beta^2 + \alpha^2\gamma^2) + (-1 + \hat{\sigma})(\gamma^2 + \alpha^2\beta^2\hat{\sigma})}{1 + \alpha^4\hat{\sigma}} \right) \\ \frac{-1}{2\gamma(1 + \hat{\sigma})} \left( 1 - \hat{\sigma} + \frac{2(-\beta^2 + \alpha^2\gamma^2) + (-1 + \hat{\sigma})(\gamma^2 + \alpha^2\beta^2\hat{\sigma})}{1 + \alpha^4\hat{\sigma}} \right) \\ \frac{r_b}{2\mu(1 + \hat{\sigma})} \left( -\frac{1}{2} - \hat{\sigma} \log(\beta) + \frac{2\alpha^4 + \beta^2 + \alpha^2\gamma^2(-2 + \hat{\sigma}) + (-1 + \hat{\sigma})(\alpha^2 - \gamma^2 + \frac{\hat{\sigma}}{2}(-\alpha^2\beta^2 + \gamma^2))}{2(1 + \alpha^4\hat{\sigma})} \right) \\ \frac{r_b}{2\mu(1 + \hat{\sigma})} \left( \frac{1}{2} - \hat{\sigma} \log(\beta) + \frac{(-1 + \hat{\sigma})(\alpha^2 - \gamma^2 - \frac{\hat{\sigma}}{2}(-\alpha^2\beta^2 + \gamma^2)) - (-2\alpha^4 + \beta^2 + \alpha^2\gamma^2(2 + \hat{\sigma}))}{2(1 + \alpha^4\hat{\sigma})} \right) \\ \frac{\gamma}{2\mu(1 + \hat{\sigma})} \left( \frac{\hat{\sigma}}{\gamma^2} + \frac{-\frac{\beta^2}{\gamma^2} + \alpha^2(-2 + \hat{\sigma}) + (-1 + \hat{\sigma})(-1 + \frac{\hat{\sigma}}{2}(1 + \beta^4))}{1 + \alpha^4\hat{\sigma}} \right) \end{bmatrix}$$

$$\delta_n = (1 - \alpha^2)^2 (1 - n^2) - (\alpha^{-2n} + \alpha^2\hat{\sigma}) (\alpha^{2n} + \alpha^2\hat{\sigma})$$

$$B_n = \begin{bmatrix} 1 - \alpha^2 & -\frac{1 + \alpha^{2-2n}\hat{\sigma}}{1 + n} \\ -\frac{1 + \alpha^{2+2n}\hat{\sigma}}{1 - n} & 1 - \alpha^2 \end{bmatrix}$$

$$A_n(r) = \begin{bmatrix} \gamma^n (1 + n) (2 - n + \beta^{2+2n}\hat{\sigma} - \beta^2 (1 - n)) & \gamma^{-n} (1 - n) (2 + n + \beta^{2-2n}\hat{\sigma} - \beta^2 (1 + n)) \\ \gamma^n (1 + n) (-n - \beta^{2+2n}\hat{\sigma} + \beta^2 (-1 + n)) & \gamma^{-n} (-1 + n) (n - \beta^{2-2n}\hat{\sigma} - \beta^2 (1 + n)) \\ \frac{1}{2\mu} \gamma^n r (\hat{\sigma} (1 - \beta^{2+2n}) + (-1 + \beta^2) (1 + n)) & \frac{1}{2\mu} \gamma^{-n} r (\hat{\sigma} (1 - \beta^{2-2n}) + (-1 + \beta^2) (1 - n)) \\ \frac{1}{2\mu} \gamma^n r (\hat{\sigma} (-1 + \beta^{2+2n}) + (-1 + \beta^2) (1 + n)) & \frac{1}{2\mu} \gamma^{-n} r (\hat{\sigma} (1 - \beta^{2-2n}) + (1 - \beta^2) (1 - n)) \\ \frac{1}{2\mu} \gamma^n (1 + n) (-1 - n + \hat{\sigma} + \beta^{2+2n}\hat{\sigma} + \beta^2 (-1 + n)) & \frac{1}{2\mu} \gamma^{-n} (1 - n) (-1 + n + \hat{\sigma} + \beta^{2-2n}\hat{\sigma} - \beta^2 (1 + n)) \end{bmatrix}$$

$$L = \frac{1}{2} \begin{bmatrix} 1 & 1 \\ 1 & -1 \end{bmatrix}$$